ERF2011_165

COMPUTATIONAL INVESTIGATION OF HUB DRAG DECONSTRUCTION FROM MODEL TO FULL SCALE

Rajiv Shenoy rajiv.shenoy@gatech.edu
Marlin Holmes mholmes7@gatech.edu
Marilyn J. Smith marilyn.smith@ae.gatech.edu
Narayanan M. Komerath narayanan.komerath@ae.gatech.edu
Daniel Guggenheim School of Aerospace Engineering
Georgia Institute of Technology, Atlanta, Georgia, 30332-0150, USA

Abstract

Parasite drag on rotorcraft can become a crucial factor in forward flight, especially for high speed flight. Prior evaluations of the ability of computational methods to predict hub drag have focused on the ability of these solvers to match model scale experimental data, but the codes have not been examined for full scale conditions. Using an unstructured computational method, the sources of hub drag on a moderately complex model are deconstructed and examined for model and full scale configurations and flight conditions. Correlations with a model-scale wind tunnel test and theoretical data are provided to confirm the appropriateness of the initial grid. Unlike prior efforts, grid adaptation across the overset meshes permits grid refinement where needed and minimizes the grid cost. It has been observed that for the moderately complex hub evaluated that grids developed for the model scale analysis can not be applied directly to a full-scale analysis. Deconstruction of the drag illustrates that evaluation of the Reynolds number for each component to evaluate its impact on drag, as well as consideration of changes in the interference effects, are required when scaling results from model to full scale, even for static (nonrotating) configurations. Velocity scaling for rotating hubs must also be considered; scaling to similar advance ratio rather than rotor angular velocity appears to be more appropriate. Estimation of the interference drag for rotating hubs must consider the Magnus effect, which appear to directly influence the nonlinearities observed in scaling the drag.

NOMENCLATURE

C_D	drag coefficient
c_p	pressure coefficient
d	cylinder diameter, m
D	hub assembly diameter, m
M	Mach number
R	(full) rotor blade radius, m
Re	Reynolds number
V	velocity, m/s
u/U	nondimensional velocity in the x-direction
x, y, z	Cartesian streamwise,radial and normal lengths, m
y^+	dimensionless wall spacing
μ	advance ratio, U/Ω R

INTRODUCTION

Parasite drag on rotorcraft can become a crucial factor in forward flight, especially for high speed flight [1, 2], limiting the range, maximum speed, and payload of the vehicle. Reduction in parasite drag can improve vehicle stability and control [3] and significantly decrease vibrational and blade loads to reduce vehicle weight and extend the rotor blade life [4]. Hub assemblies for single main rotor helicopters can contribute nearly 25%-30% of vehicle parasite drag, while hub assemblies for coaxial rotors can contribute as much as 50%, as is the case with the XH-59 [5]. Therefore, reduction of the drag in the design of hub systems is critical to the success of new high-speed rotorcraft design. In order to achieve these goals, the drag sources associated with complex hubs must be thoroughly investigated, understood, and reliably predicted using analysis and design tools. Fundamental experimental studies of hub drag [5–9] are underway, accompanied by analyses of the ability of computational fluid dynamics (CFD) tools to predict these complex flows. These studies are all characterized by the fact that they are accomplished on models that are a fraction (1/5 - 1/4 scale) of the full scale rotor hub. Thus, it is imperative that the scaling of these complex systems, including rotational and interference effects also be understood.

Potsdam and Le Pape [10] have identified several mechanisms of hub drag separation that lead to poor CFD results, and further complications arise when moving from the incompressible to the compressible flight regime, and transition from laminar to turbulent flow must also be considered. Wind tunnel studies on compound rotorcraft show large uncertainty in the quantification of interference drag [11], a phenomenon that needs to be thoroughly understood in order to obtain consistency in hub drag design. Design estimates based on classic bluff-body drag may not be directly applied to rotorcraft hubs since such configurations have components that move relative to one another, resulting in varying interference drag. Another consideration is that for some flight conditions, individual geometry components (swashplate, pitch links, driveshaft, shanks, etc.) lie in the transitional Reynolds number regime.

Wake and his coauthors [5] have investigated 1/4 scale faired hubs for the X2 Technology^{TM} Demonstrator aircraft using

an unstructured computational solver. These simpler faired elliptical geometries can prove to be challenging because of the difficulty of predicting separation (and potentially transition). The focus of this effort was to investigate the impact of aerodynamic fairings on drag for the dual hub configuration. Using a grid refinement study, Wake's team was able to obtain agreement with experiment within 15% for their tetrahedral grids and within 3% for their hexahedral grids, and matched within 8% the configuration changes obtained by two experimental studies. The configuration was static and did not include components such as root stubs or hardware in the analysis. A follow-on study in 2011 by Sikorsky [12] using another unstructured method confirmed the overall findings of their initial undertaking.

Bridgeman and Lancaster [8] have studied a 1/5 scale Bell rotor hub and fuselage both experimentally and computationally. Using an extensive grid independence study, they found that total drag predictions within 5%-10% of experimental values using an unstructured solver could be achieved for the non-rotating hub-fuselage configuration, depending on the grid resolution. Details such as hardware, pitch links, and root stubs were included in the computational model; a breakdown of the individual contributions of these components was not part of the focus of this work. A follow-on paper [7] indicated that comparable results could be achieved by any of the unstructured solvers that were evaluated, including the solver utilized in the present study. Additional reporting to include a rotating hub are planned for 2012 [9].

Ortega et al. [6] have studied a 1/4 scale moderately complex rotor hub with the focus of deconstructing drag. Both experimental and computational efforts have been undertaken to study integrated drag quantities and the complex near wake. Computations with an unstructured solver, including details such as the hardware, pitch links, etc., have yielded drag correlations within 5%-7% of experimental values for both static and rotating hub configurations. These computations also utilized grid adaptation, and the computations were able to resolve the near wake features (1 hub diameter downstream), as compared with experimental particle image velocimetry (PIV) data.

The current study builds upon these prior efforts and extends the knowledge of hub drag in several areas not considered by the prior art. Using computational methods, the sources of hub drag on a moderately complex model are deconstructed and examined for model and full scale configurations and flight conditions. Correlation with a model-scale wind tunnel test and theoretical data are provided to confirm the appropriateness of the initial grid. Grid adaptation across the overset meshes permits grid refinement where needed and minimizes the grid cost.

Details of the Investigation

Configuration

A generic 1/4-scale four-bladed hub, representative of a UH-60A hub, has been experimentally and computationally evaluated. The model (Fig. 1) consisted of four pitch links, a swashplate and shaft, connecting hardware, and two hub plates, offset by blocks to secure four capped rotor shanks. Static wind tunnel evaluations of the model were conducted for zero degrees angle of attack and varying azimuthal angles from 0° to 75° in 15° increments. An azimuthal orientation of 0° corresponded to an upstream facing hub shank parallel to the free stream velocity. Rotational effects were evaluated at a nominal 240 rpm at various free stream velocities. Load cell data were collected at 1000 Hz and time averaged to provide estimates of the drag coefficient. Details of the model scale experimental and computational evaluations can be found in Ortega et al. [6].

A modified version of NASA's ROBIN configuration used by Schaeffler et al. [13] was selected to obtain the influence of the fuselage on the hub inflow. The fuselage grid that was applied in this study ensured that the predicted free-air drag was within 2% of that obtained by other CFD codes in Schaeffler et al. [13], verifying that the grid was sufficient for these simulations. For the full-scale tests, the fuselage is scaled to length of the UH-60A fuselage, and hub was independently scaled and positioned to corresponding UH-60A hub location.

In this analysis, four specific configurations are presented to illustrate the scaling. Two static configurations with the hub oriented at 0° and 45° azimuth are examined, in addition to two rotating configurations. The flight conditions chosen were that of the C8534 flight test counter [14, 15], which has emerged as a standard computational rotor correlation case. C8534 provides a high speed test case that permits a total Reynolds number (Re) scaling of a factor of 28 with respect to the model, as tested.

The two rotating cases are scaled from the same model scale case, but result in two full scale cases to examine velocity scaling. In one instance, the rotor rotation rate is kept constant at the 240 rpm evaluated at the model scale. This case, known hereafter as *Rot1*, has an advance ratio, $\mu = 0.395$. The second case, known as *Rot2*, maintains the scale model advance ratio, $\mu = 0.152$ with an increase in the rotor angular velocity to 623 rpm. The details of the scaling and free-stream conditions used for all cases are given in Table 1.

Table 1: Scaling Information for the model and full size test hubs.

	Model Scale	Full Scale
Hub diameter (d, m)	0.4862	1.7017
Density $(\rho, kg/m^3)$	1.1901	1.07317
Velocity $(V, m/s)$	8.941	81.23
Reynolds number (Re)	0.291×10^6	8.135×10^6

Computational Methodology

The computational investigations have been conducted using FUN3D, an unstructured Reynolds-averaged Navier-Stokes (RANS) methodology with overset adaptative grid capability developed by NASA [16]. Overset capability has been successfully used in FUN3D for compressible and incompressible rotorcraft applications, for example Refs. [6, 17, 18]. Since both static and rotating hub conditions are examined, the grid has been generalized such that a near-body grid of the

hub is overset with a background grid of either a wind tunnel test section or a fuselage. Because the optimal grid changes with each configuration, an anisotropic grid adaptation strategy that smoothly transcends overset grid boundaries [19, 20] is needed to minimize the numerical dissipation to more accurately capture the unsteady loads and wake features.

A hybrid RANS and large eddy simulation (LES) turbulence method [21] with 25 sub-iterations per time step was applied to capture the unsteady flow field for both static and rotating configurations. The dimensional time step was selected equivalent to a 1° azimuthal sweep of the 240 rpm rotating hub for all simulations except for the *Rot2* simulation where time step advancement was performed using its equivalent to a 1° azimuthal sweep.

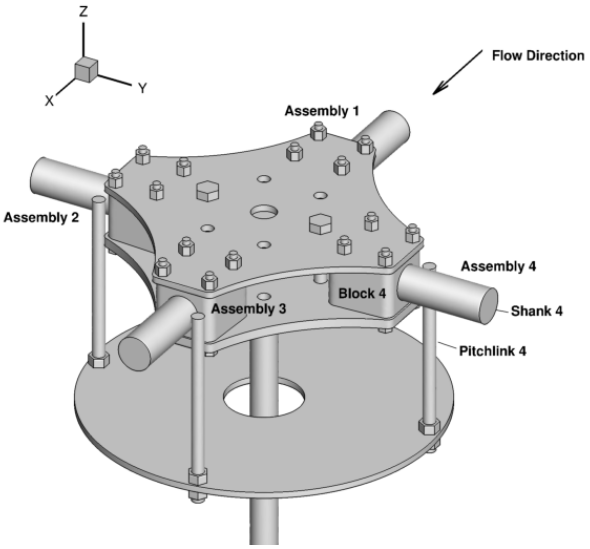

(a) 0° orientation

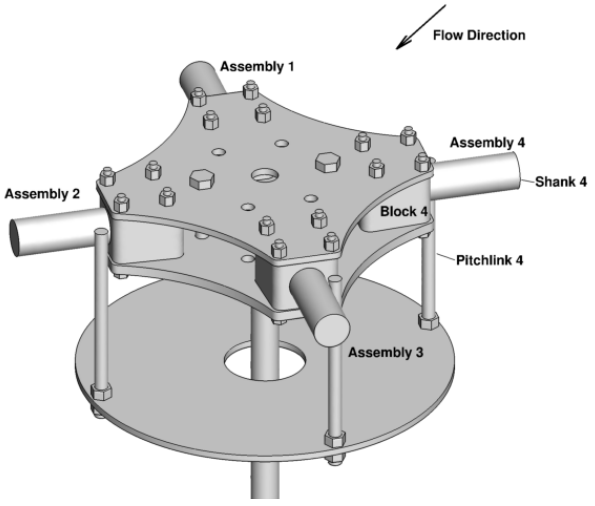

(b) 45° orientation

Figure 1: Hub configuration detailing components and orientation.

An initial grid was generated using VGRID [22]. Grid studies were conducted on the near-body hub grid using grid generation options such as off-body grid sources, anisotropic stretching, and increased boundary layer clustering. After this study was completed, the final near body mesh included a boundary layer grid with 35 cells in the normal direction and with a maximum y^+ of about 0.35 and 1.0 for all model and full scale simulations, respectively. In order to ensure that the grid is sufficient for the full-scale simulations, the boundary layer grid *must* be designed for the full-scale boundary layer, rather than relying on a simple scaling multiplier applied to the model scale grid. The application of the latter can result in significant errors at higher Reynolds number. A static simulation sweep on the present geometry indicated that the difference in drag predicted by experiment and computational increased linearly as a function of free stream velocity squared (V_∞^2) when the boundary layer grid is not tuned to the largest Reynolds number. The near body grid is depicted in Fig. 2. These grid studies also confirmed that off-body refinement and adaptation are necessary to capture the near-wake contributions of pressure drag at the higher Reynolds number.

Time-dependent anisotropic grid adaptation for the overset mesh *external* to the boundary layer was performed for all conditions evaluated in this study. An adaptation strategy based on vorticity magnitude was applied to detect local errors over a specified periodic time interval (1 revolution or 360 time steps). For uniformity between the scaled simulations, the same level of vorticity magnitude is used to form the adaptation metric. A summary of the grid size growth during adaptation for the different model and full-scale simulations is given in Table 2. Based on the different unsteady wakes that arise with each condition investigated, the grid size increases independently, and as expected, the more complex wakes arising from the rotating scenarios require additional mesh fidelity than their static counterparts.

Table 2: Effect of adaptation on the grid size for various scale simulations.

	Model Scale	Full Scale
Static hub at 0° orientation	42.3%	59%
Static hub at 45° orientation	44.1%	84.6%
Rotating hub at 240 rpm	75.7%	91%
Rotating hub at 623 rpm	-	87.2%

Correlation with Model Scale Experimental Data

Before any analysis can be accomplished at different scales, the grid and analysis fidelity must be verified. This was achieved by comparisons with experimental data obtained at the model scale static and rotating conditions. Grid adaptation, as described previously, ensured that the wake features, in particular for the near body, were adequately resolved. Fig. 3 confirms that with the adapted grid, the drag correlates well with the experimental data, including a preliminary assessment of the Reynolds number scaling effects, as defined by increasing tunnel dynamic pressure. The computational and experimental results were within 10-11% (usually within 5%) for all static azimuths, as well as for the rotating hub. The necessity of the grid adaptation is also illustrated in Fig. 4 which compares the time-averaged wake velocity deficits at a point one hub diameter downstream of the hub.

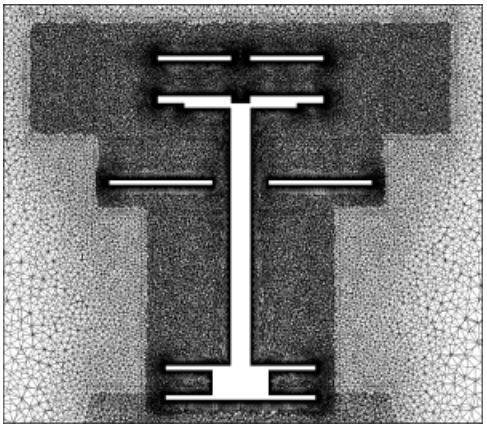

(a) Longitudinal plane passing through the hub center

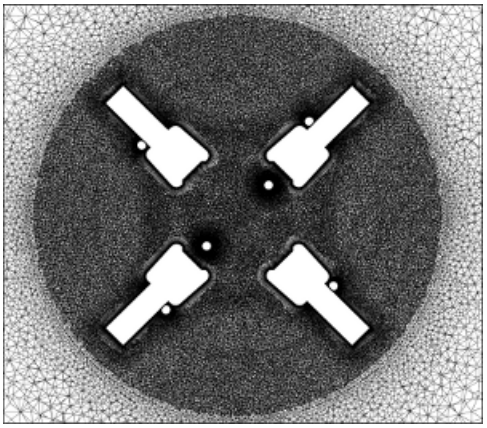

(b) Lateral plane passing between the hub plates

Figure 2: Sliced views of composite overset grid.

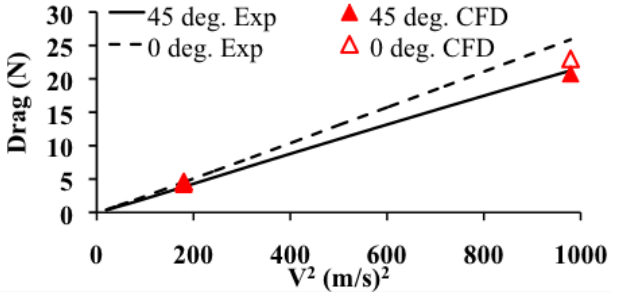

Figure 3: Correlation between experimental load cell and CFD data for the 0° static hub model

ANALYSIS

The full-scale configuration examined at flight conditions based on the UH-60A C8534 counter [15], provides an order of magnitude increase in the global Reynolds number compared to the model scale experiment. To illustrate the Reynolds number effects, two full-scale rotating conditions to provide a variation based on rotating speed and advance ratio were also analyzed along with the static hub orientations are discussed.

Global and Component Drag

The combined pressure and viscous drag has been gathered for the total configuration and each of the components and time-averaged over several periods of cyclic behavior, as appropriate to each case. Table 3 and Fig. 5 illustrates the change in the drag when moving from model to full scale.

There is a significant decrease of approximately 20% from the static configurations when the full scale configuration is analyzed. This reduction decreases for the rotating hub at the same angular velocity (11% drag reduction) and the drag is approximately equivalent when the same advance ratio is modeled at both scales, which required an increase in the model rotor angular velocity.

Figure 5 indicates the importance of the different components in the drag. The block assemblies are the primary contributors to drag, resulting in 20%-30% of the total drag, followed by the driveshaft which contributes 15%-20% of the drag. Not unexpectedly, the hub mount, hub and swash plates supply the least overall drag. The importance of modeling the details is clear as the hardware (bolts, nuts, etc.) contribute 10%-15% of the drag.

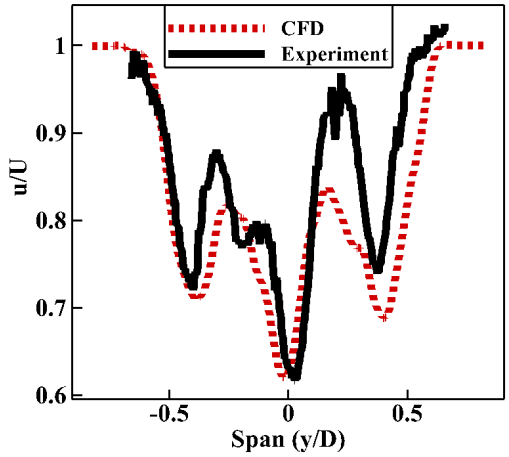

(a) Static hub at 0° orientation

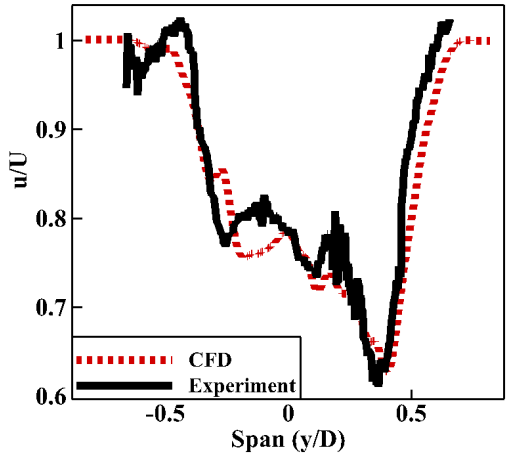

(b) Counter clockwise rotating hub at 240 rpm

Figure 4: Comparison of time-averaged PIV and CFD wake velocity deficit along the tunnel axis. From Ref. [6].

Table 3: Comparison of global (total) drag coefficient.

	Model Scale	Full Scale
Static hub at 0° orientation	0.98	0.78
Static hub at 45° orientation	0.89	0.74
Rotating hub at 240 rpm	1.07	0.95
Rotating hub at 623 rpm	-	1.10

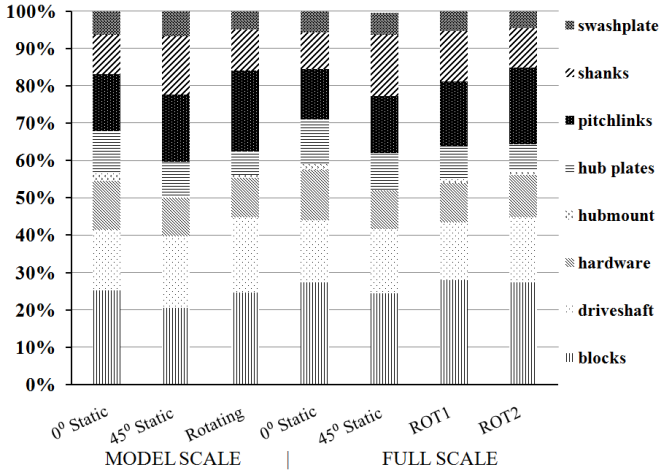

Figure 5: Component drag contributions to hub drag .

Experimental and computational analysis [6] at the model scale identified similarities in the static 45°orientation and the rotating configuration, as confirmed by the total drag coefficient (Table 3) and in a later discussion by the surface pressure coefficient (Figs. 8(a) and 9(a)). However, this similarity between the two configurations does not extend to the full scale configuration. The reasons for the change are explored by examination of the components and hub wake.

Analysis of the change in the individual component contributions to drag provides some insight into the cause of the differences. The actual drag coefficient change (Fig. 6(a)) yields the overall change, but the importance of each change is more readily observed by the percentage drag change in Fig. 6(b). Approximately half of the components contribute a small percentage change in the drag (within 2% - 4%) no matter what the configuration, static or rotating. For the components that are flat plates of various shapes, namely the swashplate and the hub mount, the drag reduction is related primarily to the viscous (skin friction) drag as Reynolds number increases [23].

Five components in particular, the blocks, hub plates, driveshaft, shanks, and pitchlinks, do not conform to the relatively constant trend. These components are notably comprised of primarily bluff bodies, three of which are circular cylinders. Further analysis of the cylindrical components is compared with experimental results from Hoerner [24]. Due to the installation, most of these cylindrical components have "wall-like" ends and are of sufficient aspect ratio that they can be considered as essentially two-dimensional bodies, as per Hoerner's experimental assessment. Table 4 lists the Reynolds numbers and drag coefficients achieved from the analysis of the static orientation at 0° azimuth. The critical Reynolds number (Re_c) for cylinders in a cross-flow is approximately 300,000-400,000. Despite a subcritical Reynolds number at the model scale, the driveshaft obtains a drag value about 30% lower than then experimental drag prediction of 1.18. This is attributed to interference effects from the swashplate and the pitchlinks. At full scale, the driveshaft drag reduces and is within the critical *Re* range where the drag reduces from 1.18 to approximately 0.3 over a small range of *Re*. Similar lower drag trends are observed with the pitchlinks, which can be attributed to interference drag arising from their respective assemblies (see Fig. 1 (a)). Pitchlink 4 obtains the closest cylinder drag in comparison to the experimental value at both model and full scales. This is not unexpected given its orientation where minimal interference effects and nearly unperturbed free stream flow are encountered. Shank interference causes a reduction in drag at the model scale obtained for pitchlinks 1 and 2; pitchlink 1 is affected by the presence of its shank and the assembly of pitchlink 2 is on the leeward side of its shank. Pitchlink 3 shows interference effects due to its location farthest downstream with respect to other components. Overall, the influence of scaling of the pitchlinks is negated due to the compensating interference effects, and this was observed at all static locations (e.g., see Fig. 6). Shanks 2 and 4, which should nominally compare with Hoerner at drag values of 1.18 and 0.3-0.4 at model and full scales respectively, encounter interference and/or finite aspect ratio effects that result in reduced drag from theory.

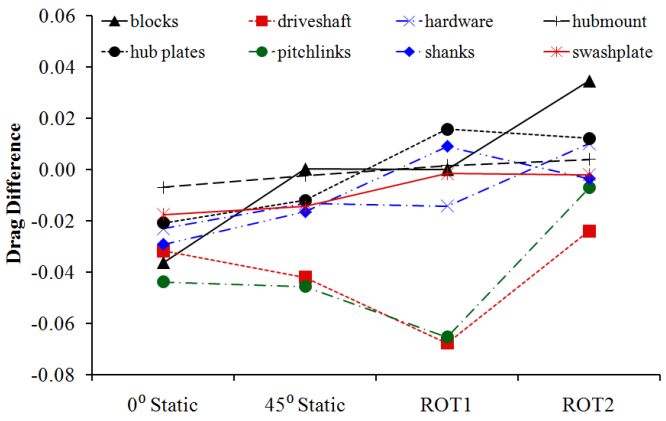

(a) Drag coefficient change

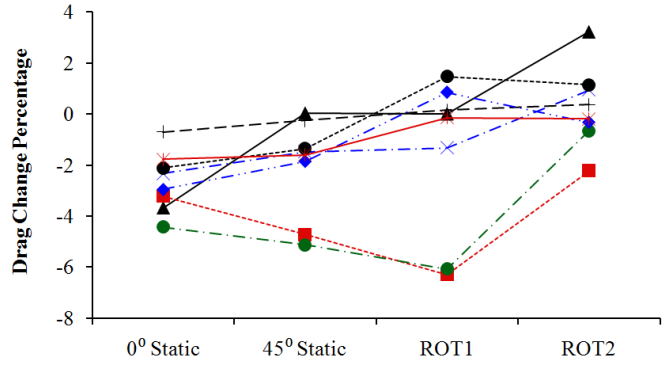

(b) Percentage drag change

Figure 6: Hub drag detailing differences between full and model scales (Delta Drag = Full Scale - Model Scale).

For the rotating cases, the decrease in drag is not as significant as that for the static configurations, and improvement in drag due to scaling diminishes as the rotation speed increases, indicating the presence of the "Magnus" effect [24], as well as changes in the friction drag and interference drag, which are discussed later. The cylindrical components are again primary components that drive the drag change with scaling. The rotating driveshaft follows the trend of the static driveshaft, but with a slight increase in drag. The scaling of the system puts the velocity ratio of the driveshaft between 1 and 2, where the Magnus effect of a rotating cylinder with a single end plate (similar to the hub geometry) predicts an approximately comparable drag increase due to the creation of a side force.

Table 4: Drag tabulation for cylindrical components at a static 0° azimuth orientation.

	Model Scale		Full Scale	
Component	Re_d	C_D	Re_d	C_D
Driveshaft	15,200	0.8004	425,000	0.5789
Pitchlink 1	7,600	0.7382	213,000	0.4628
Pitchlink 2		0.8147		0.4913
Pitchlink 3		0.3259		0.2781
Pitchlink 4		0.9836		0.5935
Shank 2	21,000	0.6057	584,000	0.3793
Shank 4		0.5197		0.2982

Table 5: Average drag tabulation for rotating cylindrical components.

Component	Driveshaft	Pitchlinks	Shanks
Model	1.0761	1.1117	0.3875
Full Scale (rot1)	0.6655	0.7202	0.3762
Full Scale (rot2)	0.8623	0.9720	0.3392

Interference Drag

Component drag deficits for the static models lie between 17% and 72% for the model scale, and between 50% and 76% for the full scale. The individual component analysis does not account for these large deficits, thus interference drag is clearly present, and the effects of interference are more prevalent for the full scale model.

The presence, or lack thereof, of interference drag can be readily observed using surface pressure coefficients. Figures 7, 8, and 9 compare the model and full scale surface pressures for the 0°static, 45°static, and rotating configurations, respectively. Pressure contours that remain consistent along a component and regardless of scaling indicate minimal interference effects are present. This permits the application of component drag characteristics, such as those found in Hoerner [24] during design. As discussed earlier, for the static configurations, the largest drag reductions occur for the cylindrical components as they move from the subcritical to critical transition based on the component diameter-based Reynolds number.

The static hub configurations appear to scale with little change in the interference drag, as observed in Figs. 7 and 8, in concert with Fig. 6. The changes in each component are primarily explained through known Reynolds number effects.

The rotating hub configurations appear to scale more nonlinearly, and are clearly influenced by the angular rotation rate. The largest change is due to the interference drag on the block assemblies, which model the hub/rotor interface, and account for an 8% increase in the drag. The change in the interference drag can clearly be observed in Fig. 9. The character of the pressure contours on each of the visible portions of the blocks are changing both from the model scale to full scale, as well as the rotation rates for the two full scale models.

The nonlinearity associated with interference drag for the rotating hubs is clearly illustrated in Fig. 10. Here, the rotating cases are examined in planform images for the mid-plane of the hub using identical contour levels. Overall, greater mixing is observed in the full scale flow fields (hence vorticity levels are lower) due to increase in the Reynolds number creating a more turbulent wake. The change in pressure coefficient and shed wake are clearly related when comparing Figs. 10 and 9.

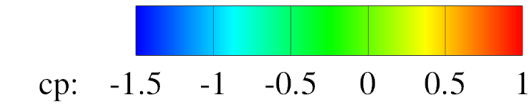

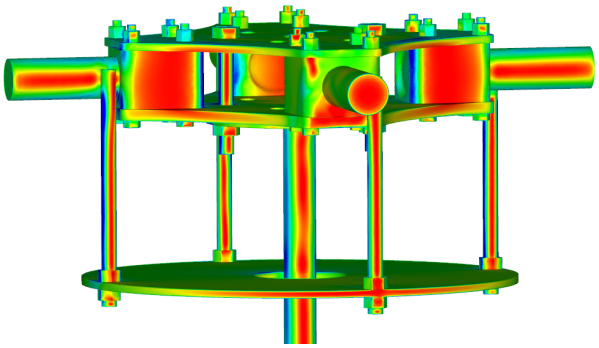

(a) Model Scale

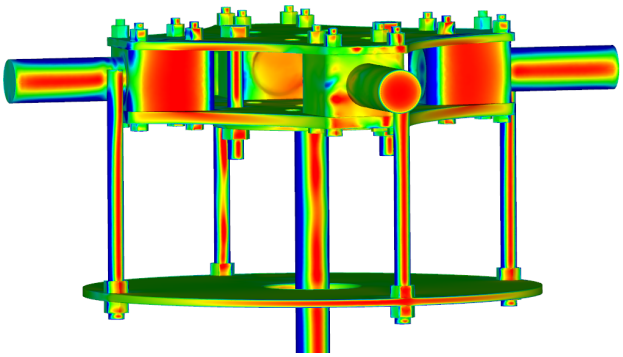

(b) Full Scale

Figure 7: Surface pressure coefficient distribution on the static rotor hub at 0° azimuth. View is approximately 90° counterclockwise from flow direction in Fig. 1(a).

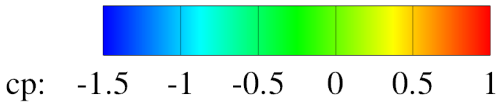

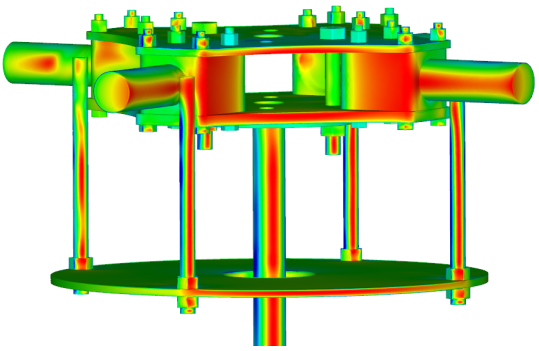

(a) Model Scale

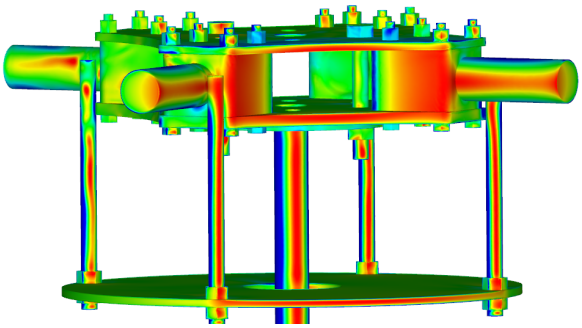

(b) Full Scale

Figure 8: Surface pressure coefficient distribution on the static rotor hub at 45° azimuth. View is approximately 90° counterclockwise from flow direction in Fig. 1(b).

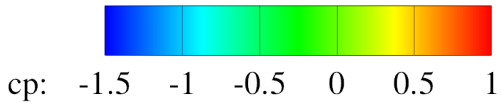

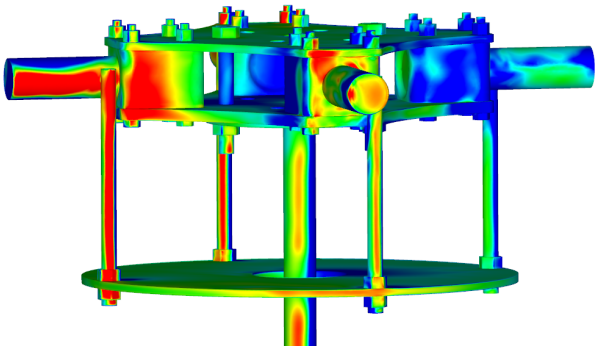

(a) Model Scale

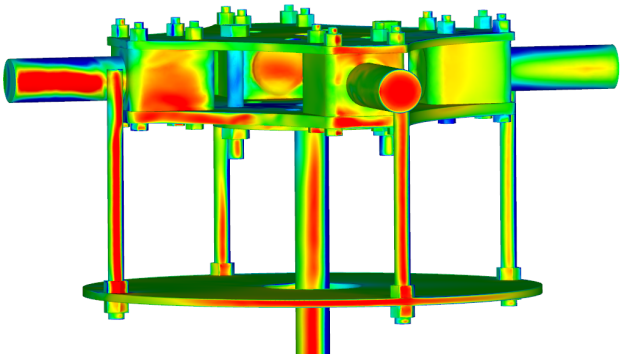

(b) Full Scale Rotating at 240 rpm

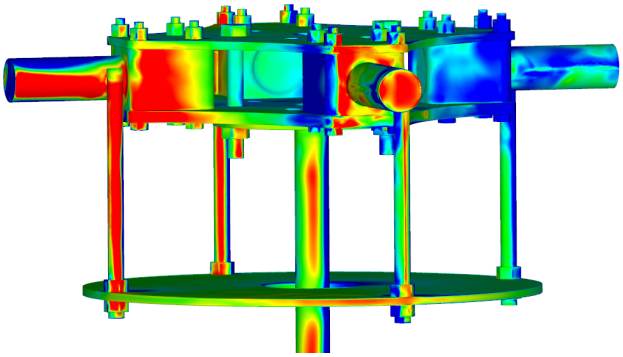

(c) Full Scale Rotating at 623 rpm

Figure 9: Surface pressure coefficient distribution on the rotating rotor hub. View is approximately 90° counterclockwise from flow direction in Fig. 1(a).

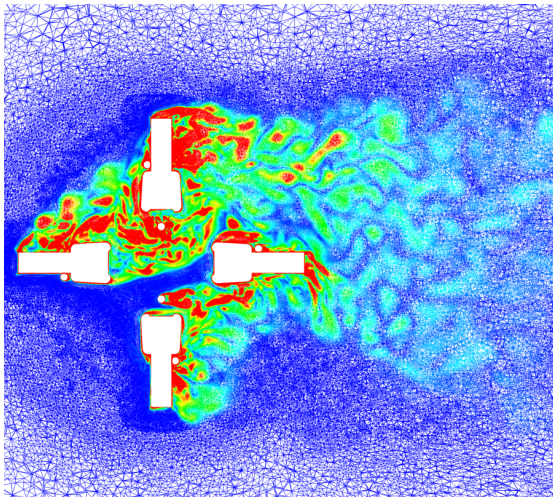

(a) Model scale

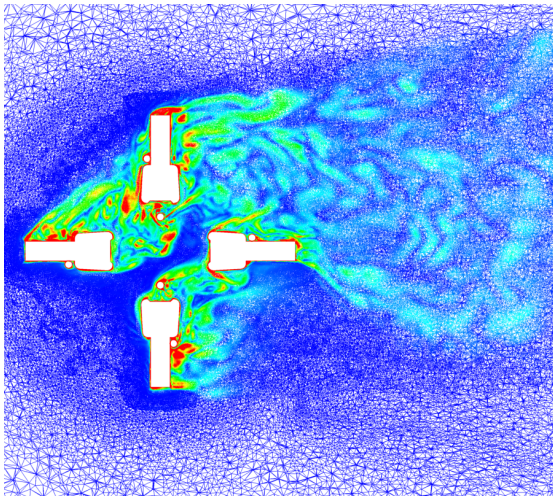

(b) Full scale rotating at 240 rpm

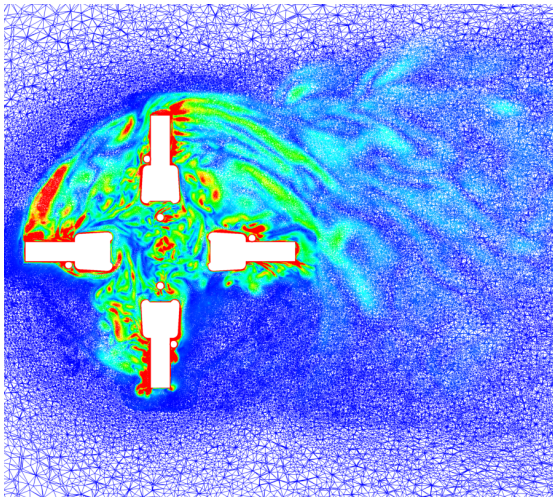

(c) Full scale rotating at 623 rpm

Figure 10: Vorticity magnitude contours of the mid-plane planform view (looking down) of the rotating rotor hub. The free stream velocity is from the left.

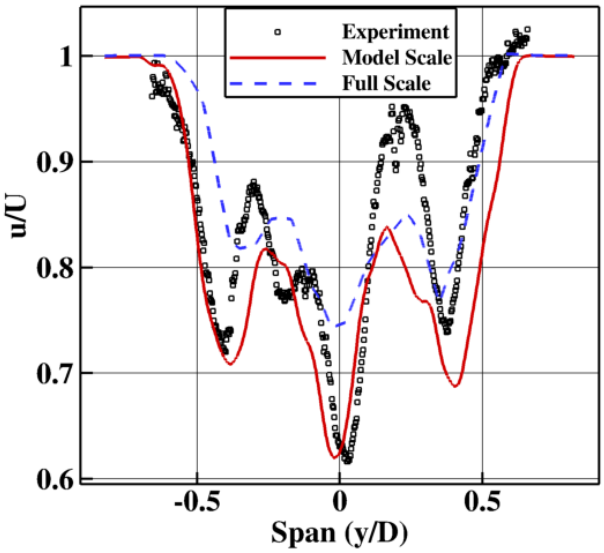

(a) Static hub at 0° orientation

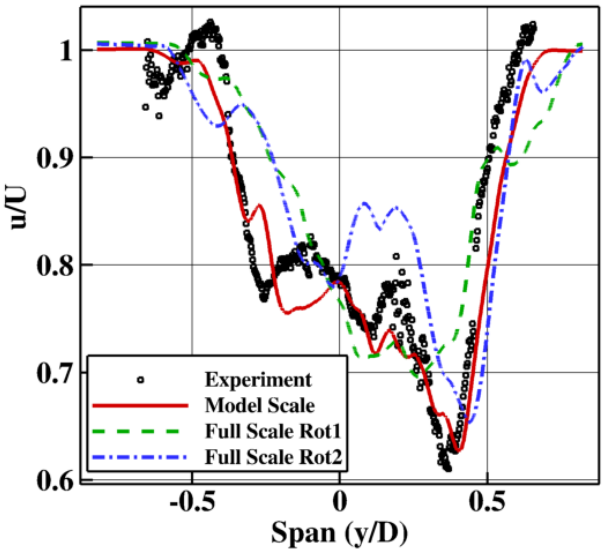

(b) Counter clockwise rotating hub

Figure 11: Comparison of time-averaged PIV and CFD wake velocity deficit along the tunnel axis including scaling.

The model scale (Fig. 10(a)) is rotating at 240 rpm, and the differences in the shed vorticity from the shanks due to the change in advance ratio are clearly observed when comparing to the full scale in Fig. 10(b). The flow field for the increased rotation rate of 623 rpm (to match the model scale advance ratio) contains much clearer shank tip vortices that may be attributable to the increased rotation rate. The flow field in Fig. 10(b) has some of the same characteristics with the model scale with respect to the relatively unperturbed "flow through" in the hub region, not observed at the higher rotation rate. The vortical content in the wake region clearly shows a shift to the right (top) side of the hub in the full scale runs, and increasing the rotational rate appears to increase this shift. This wake shift is confined to scaling of the rotating system, as the static configuration at 0° azimuth does not show a shift in the wake

velocity deficit (Fig. 11(a)), while the rotating system indicates that the shift is present (Fig. 11(b)). This confirms the presence of the Magnus effect postulated earlier, as the counterclockwise rotation biases the wake towards the right (top) of the figure. Drag varies in these situations with the ratio of the local velocity to the free stream velocity, encountering first a reducing drag as separation reduces, then increasing drag as the side force generated increases (the range of these data). Evaluation of the $C_D(C_Y^2)$ behavior with C_Y^2 shows a fairly linear response, parallel to induced theory [24]. This Magnus effect appears to be the primary cause of the increased interference drag of the block assemblies. Qualitatively, the response of the system appears to follow the known trend, and further quantitative analysis is warranted.

There are clearly discernible differences in the grid adaptation in the near and far wakes (overset near body and background grid) with each rotating configuration. These grid modifications from the initial grid and simulation (as illustrated by an initial simulation in Fig. 12) are key to capturing the shed wake; this bias and other wake shedding characteristics are not known a priori to the simulation. The effect of grid adaptation with the global drag is noted in Table 6. Since, the difference in global drag from the second adaptation iteration yields less than 1% difference, grid independence (with respect to drag) is established after the first adaptation cycle. With the first adaptation iteration, total drag overall was refined by as much as 16%. Given the increase in the number of mesh points with each adaptation cycle (as much as 50% on the second adaptation iteration), further adaptations were deemed impractical for the practicing engineer.

Table 6: Effect of adaptation on drag prediction for full scale simulations.

Adaptation Iteration	1	2
Static hub at 0° orientation	+3.3%	-0.47%
Static hub at 45° orientation	+15.8%	+0.77%

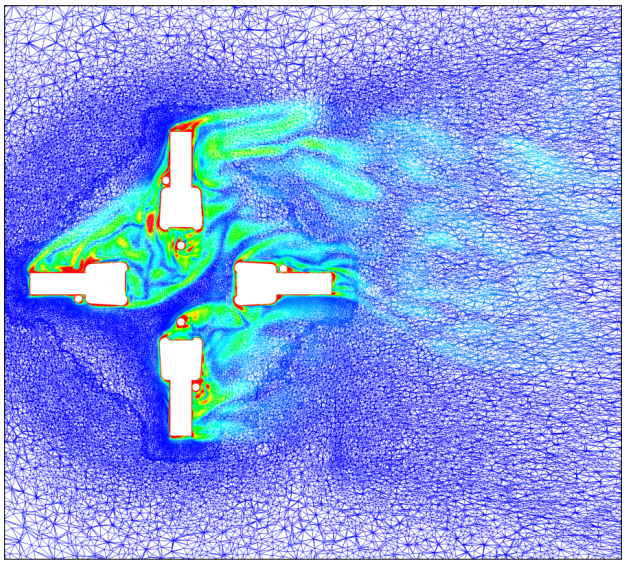

Figure 12: Initial grid and vorticity magnitude contours of the rotating rotor hub for full scale rotating at 240 rpm.

Concluding Remarks

A computational analysis of a moderately complex rotor hub at 1/4 geometric model scale and full scale has been undertaken. For the full scale configuration, analyses at different velocities provide a further insight into Reynolds number scaling. Correlation with experimental data at the model scale, as well as a grid study, provided confidence in the methodology's capability to predict the integrated force and near-wake characteristics of the configuration. Analysis of the individual components provides guidance to the engineer on the behavior of the components when changing dimensional and velocity scales.

Observations from the current analysis include:

1. The boundary layer and near body grid should be designed for the viscous characteristics of the highest Reynolds number calculation. Computations on one configuration indicate that the error appears to increase linearly with the increase in Reynolds number.

2. The application of grid adaptation that encompasses overset grids without regard to mesh boundaries, in this instance vorticity magnitude, improves the near wake and integrated load predictions, and permits an initial grid to be applied to a number of configurations without the need to develop new grids.

3. Components that are bluff bodies lead to nonlinear scaling of the drag through a combination of Reynolds number scaling effects and changes in the interference drag. For components that remain clear of the shed wakes, theoretical and experimental estimates of drag for each individual component correlate well with the computational results.

4. The determination of the interference drag for rotating bodies must include an estimation of the shift in the shed wake due to the Magnus effect. The shed wake translates as a function of the local velocity on the component surface with the free stream velocity and is clearly observed in computational evaluations.

5. When scaling the drag during rotation, the velocity scaling based on the advance ratio rather than the angular velocity of the rotor appears to a more appropriate physical scaling.

Acknowledgements

This project was partially funded by the Vertical Lift Consortium (VLC), formerly the Center for Rotorcraft Innovation and the National Rotorcraft Technology Center (NRTC), U.S. Army Aviation and Missile Research, Development and Engineering Center (AMRDEC) under Technology Investment Agreement W911W6-06-2-0002, entitled National Rotorcraft Technology Center Research Program. The authors would like to acknowledge that this research and development was accomplished with the support and guidance of the NRTC

and VLC. The views and conclusions contained in this document are those of the authors and should not be interpreted as representing the official policies, either expressed or implied, of the AMRDEC or the U.S. Government. The U.S. Government is authorized to reproduce and distribute reprints for Government purposes notwithstanding any copyright notation thereon.

References

[1] Williams, R. and Montana, P., "A Comprehensive Plan for Helicopter Drag Reduction," National Symposium on Helicopter Aerodynamic Efficiency Proceedings, Hartford, Connecticut., March 6-7, 1975, pp. 13.1-13.26.

[2] Keys, C.N. and Wiesner, R.,"Guidelines for Reducing Helicopter Parasite Drag," *Journal of the American Helicopter Society*, Vol. 20, No. 1, pp. 31-41, 1975.

[3] Hoffman, J., "The Relationship Between Rotorcraft Drag and Stability and Control," American Helicopter Society 31st Annual Forum Proceedings, Washington, D.C., May 13-15, 1975.

[4] Kerr, A., "Effect of Helicopter Drag Reduction on Rotor Dynamic Loads and Blade Life," American Helicopter Society Symposium on Helicopter Aerodynamic Efficiency Proceedings, Hartford, Connecticut, March 6-7, 1975.

[5] Wake, B. and Hagen, E. and Ochs, S. and Matalanis, C., "Assessment of Helicopter Hub Drag Prediction with an Unstructured Flow Solver," American Helicopter Society 65th Annual Forum Proceedings, Grapevine, Texas, May 27-29, 2009, pp. 2422–2433.

[6] Ortega, F., Shenoy, R., Raghav, V., Smith, M., and Komerath, N., "Deconstructing Hub Drag," AIAA-2011-3821, Applied Aerodynamics Conference, Honolulu, Hawaii, June 27-30, 2011.

[7] Bridgeman, J. and Lancaster, G., "Physics-Based Analysis Methodology for Hub Drag Prediction," American Helicopter Society 66th Annual Forum Proceedings, Phoenix, Arizona, May 11-13 2010.

[8] Bridgeman, J.O., and Lancaster, G.T., "Predicting Hub Drag on Realistic Geometries," American Helicopter Society Aeromechanics Specialists Conference, Holiday Inn Fisherman's Wharf, San Francisco, California, January 20-22, 2010.

[9] Hill, M.J., and Bridgeman, J.O, "Rotating Hub Drag Prediction Methodology," Abstract submitted to American Helicopter Society Specialists Conference on Future Vertical Lift Aircraft Design, San Francisco, CA, January 18-20, 2012.

[10] Potsdam, M., and Le Pape, A., "CFD Investigations on a NACA0036 Airfoil with Active Flow Control," AIAA-2008-3869, 4th Flow Control Conference Proceedings, Seattle, Washington, June 23-26, 2008.

[11] Keys, C.N., and Rosenstein, H.J. "Summary of Rotor Hub Drag Data," NASA CR-152080, March 1978.

[12] Ochs, S. S., Matalanis, C. G., Wake, B. E., and Egolf, T. A., "Evaluation of Helios CFD Toolset for Faired Rotor-Hub Drag Prediction," American Helicopter Society 67th Annual Forum Proceedings, Virginia Beach, Virginia, May 3-5, 2011.

[13] Schaeffler, N., Allan, B., Lienard, C. and Le Pape, A., "Progress Towards Fuselage Drag Reduction via Active Flow Control: A Combined CFD and Experimental Effort," 36th European Rotorcraft Forum Proceedings, Paper 064, Paris, France, Sept 7-9, 2010.

[14] Kufeld, R. M., Balough, D. L., Cross, J. L., Studebaker, K. F., Jennison, C. D., and Bousman, W. G., "Flight Testing of the UH-60A Airloads Aircraft," American Helicopter Society 50th Annual Forum Proceedings, Washington, D.C., May 11-13, 1994.

[15] Bousman, W. G., and Kufeld, R. M., "UH-60A Airloads Catalog," NASA TM-2005-212827/AFDD TR-05-003, August 2005.

[16] Anderson, W., Rausch, R., and Bonhaus, D., "Implicit/Multigrid Algorithms for Incompressible Turbulent Flows on Unstructured Grids," *Journal of Computational Physics*, Vol. 128, No. (2), 1996, pp. 391-401.

[17] O'Brien, D., and Smith, M., "Understanding the Physical Implications of Approximate Rotor Methods Using an Unstructured CFD Method," 31st Annual European Rotorcraft Forum Proceedings, Florence, Italy, Sep 13-15 2005.

[18] Lee-Rausch, E., and Biedron, R., "Simulation of an Isolated Tiltrotor in Hover with an Overset Unstructured Overset-Grid RANS Solver," American Helicopter Society 65th Annual Forum Proceedings, Grapevine, Texas, May 27-29, 2009.

[19] Shenoy, R., "An Adaptive Mesh Refinement Strategy for Static and Dynamic Overset Unstructured Meshes," Poster presented at the 10th Symposium on Overset Composite Grids and Solution Technology, Mountain View, California, September 20-23, 2010.

[20] Shenoy, R. and Smith, M., "Unstructured Overset Adaptive Mesh Refinement for Rotorcraft Aerodynamic Interactions," American Helicopter Society 67th Annual Forum Proceedings, Virginia Beach, Virginia, May 3-5, 2011.

[21] Lynch, C. E. and Smith, M. J., "Hybrid RANS-LES Turbulence Models on Unstructured Grids," AIAA-2008-3854, AIAA 38th Fluid Dynamics Conference and Exhibit, Seattle, Washington, June 23-26, 2008.

[22] Pirzadeh, S., "Advanced Unstructured Grid Generation for Complex Aerodynamic Applications," *AIAA Journal*, Vol. 48, No. 5, 2010, pp. 904–915.

[23] Schlichting, H., *Boundary Layer Theory*, 7th Edition, McGraw-Hill, New York, 1979.

[24] Hoerner, S. F., *Fluid Dynamic Drag*, Hoerner Fluid Dynamics, Bakersfield, 1965.